Seismicity in the western coast of the South Caspian Basin and the Talesh Mountains

Asiye Aziz Zanjani,[1] Abdolreza Ghods,[1] Farhad Sobouti,[1] Eric Bergman,[2]
Gholamreza Mortezanejad,[1,*] Keith Priestley,[3] Saeed Madanipour[4]
and Mahnaz Rezaeian[1]

[1]*Department of Earth Sciences, Institute for Advanced Studies in Basic Sciences (IASBS), P.O. Box 45195-1159, Zanjan, Iran. E-mail: farhads@iasbs.ac.ir*
[2]*Department of Physics, Center for Imaging the Earth's Interior, University of Colorado at Boulder, Boulder, CO 80309-0390, USA*
[3]*Bullard Laboratories, University of Cambridge, Madingley Road, Cambridge CB3 0EZ, UK*
[4]*Department of Geology, Tarbiat Modares University, P.O. Box 14155-175, Tehran, Iran*

GJI Geodynamics and tectonics

SUMMARY

We have studied the seismicity of the western margin of the South Caspian Basin (SCB) and the neighbouring Talesh fold and thrust belt. We have used the hypocentroidal decomposition multiple-event location technique to obtain accurate location of events recorded during 2 yr of observation. Data from a temporary seismic network in northwest Iran and other national and regional networks were combined to make an accurate assessment of seismicity in the region. Significant offshore seismicity is observed in a 50-km wide margin of the SCB. East of the Talesh Fault along the Caspian coastline, the depth of seismicity varies from 20 to 47 km. This pattern extends inland about 20–25 km west of the North Talesh Fault. This pattern of seismicity indicates that the basement slab of the South Caspian is undergoing intense seismic deformation as it is underthrusting beneath the northern Talesh, whereas the sedimentary cover deforms aseismically. The seismicity, depths, and previous focal mechanisms of the larger offshore events are consistent with low-angle underthrusting of the South Caspian floor. Within the Talesh, seismicity is mostly concentrated in the northern and southern structural arcs of the range, where deformation is more intense and complicated. Shallow crustal seismicity in the eastern flank of the Talesh is much less intense than in the western flank, where it signifies the deformation of the upper continental crust. One major observation is the lack of any significant N–S alignment of shallow epicentres inside the central Talesh to match the observed right-lateral shear deformation there. This suggests that shear deformation inside the Talesh may have a distributed nature, rather than being concentrated on a single thorough-going fault zone, as the Talesh moves northward relative to the South Caspian. We have determined a new moment tensor solution in the southwestern Talesh, with a dominant N–S trending right-lateral motion, the only solution so far confirming along-strike shear deformation in the Talesh.

Key words: Seismicity and tectonics; Body waves; Continental margins: convergent; Neotectonics; Crustal structure.

INTRODUCTION

The geometry and deformation of orogenic belts are often shaped by the presence of rigid blocks within and around them. The pattern of deformation in Iran is mostly predetermined by the shape of its borders with the surrounding rigid continental regions and by the disposition of large, relatively rigid blocks within it (Jackson *et al.* 1995). The South Caspian Basin (SCB) on the southern margin of the Eurasian Plate is a rigid basement block that has highly affected the deformation history and seismotectonics of the surrounding Caucasus, Talesh, Alborz and Kopeh Dagh mountain ranges (Fig. 1) (e.g. Berberian 1983; Jackson & McKenzie 1984; Jackson *et al.* 2002). The basin is most probably of oceanic origin and is underthrusting beneath the neighbouring continental regions to the west and south and north of it, but the degree of underthrusting on each boundary remains unknown.

*Now at: Institute of Geophysics, University of Tehran, P.O. Box 14155-6466, Tehran, Iran.
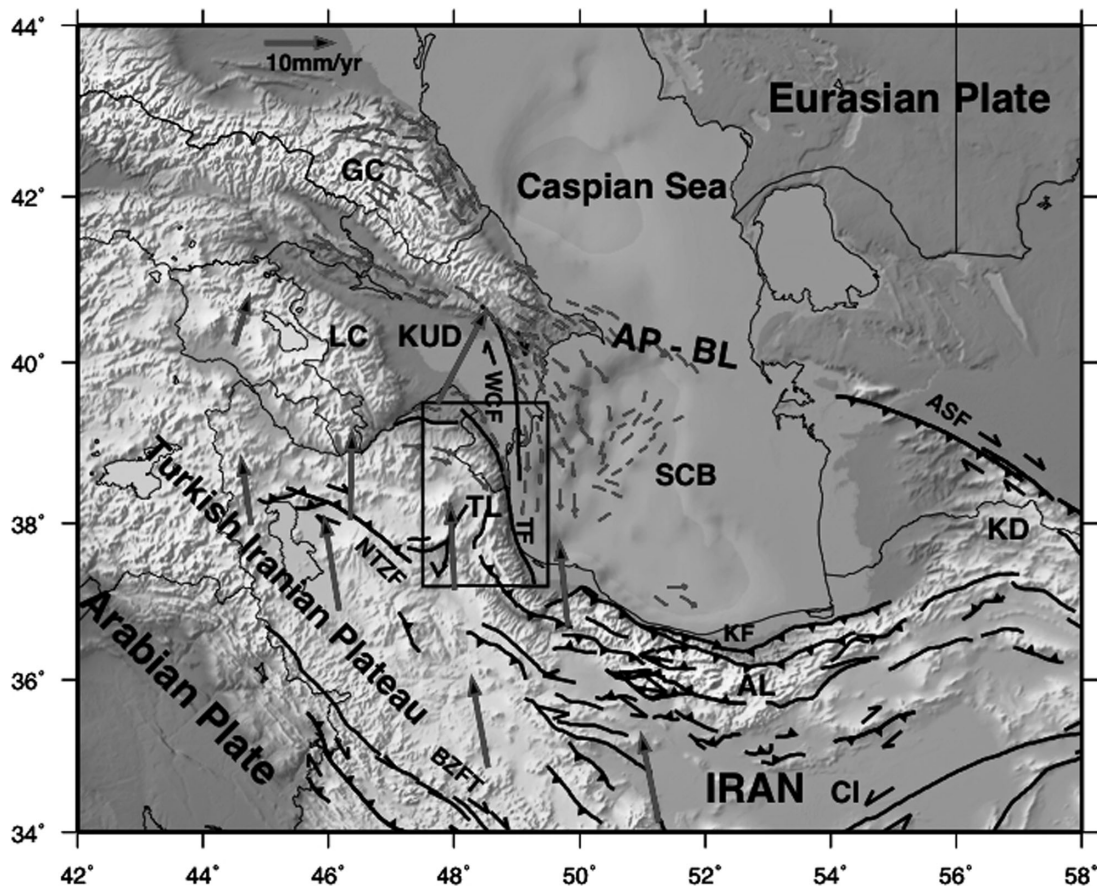
Figure 1. Shaded relief map of the South Caspian, Talesh and surrounding areas. The study area in the east of the Turkish-Iranian Plateau is shown by the black box. Faults and fold axes are shown by black and grey lines, respectively. Abbreviations: South Caspian Basin (SCB), Central Iran (CI), Talesh Mountains (TL), Greater Caucasus (GC), Lesser Caucasus (LC), Alborz Mountains (AL), Kopeh Dagh (KD), Kura Depression (KUD), West Caspian Fault (WCF), Talesh Fault (TF), North Tabriz Fault (NTZF), Khazar Fault (KF), Ashghabad Fault (ASF), Apsheron-Balkhan Sill (AP-BL). Faults are from Hessami *et al.* (2003) and Jackson *et al.* (2002). GPS vectors are from Djamour *et al.* (2011).

The SCB is considered a rigid block primarily because it lacks major intrabasin seismicity (Ambraseys & Melville 1982; Berberian 1983; Jackson & McKenzie 1984; Priestley *et al.* 1994; Jackson *et al.* 2002). Along the southwestern shoreline, most of the data on seismicity comes from regional and teleseismic networks, and there has never been an attempt to monitor microseismicity with local networks. Some relatively large earthquakes ($M_L = 5$) have been located along the western margin and offshore of the basin (Engdahl *et al.* 1998). The Talesh and Khazar reverse faults to the west and south of the basin, respectively (Fig. 1), have been identified as major active structures responsible for several destructive earthquakes in the past 1100 yr (Berberian 1983). However, due to location uncertainties, one cannot accurately attribute the seismicity to any of the known onshore (i.e. the Talesh Fault) and/or proposed offshore faults [such as the West Caspian Fault (WCF) in Fig. 1]. Current knowledge of the seismicity is inadequate to delineate distinct bounding faults separating the Caspian basement from those of the surrounding regions.

Very few reliable focal depths are available along the western margin of the basin. Fig. 2 shows 10 focal mechanisms and depths from the Harvard Centroid Moment Tensor (CMT) catalogue. For four of these events along the Iranian shoreline Jackson *et al.* (2002) determined focal solutions, as well as focal depths in the range 15–27 km (Fig. 2), which apparently represent faulting in the basement of the SCB. Likewise, evidence for seismic deformation of the

SCB's very thick (~20 km) sedimentary cover is scarce, despite the intense folding of that cover. This fact, along with the presence of decollement horizons, has been taken as evidence for aseismic deformation of the sedimentary cover (e.g. Jackson *et al.* 2002).

Earthquake focal mechanisms in the western margin of the SCB indicate N-trending west-dipping shallow-angle thrusts (Priestley *et al.* 1994; Berberian & Yeats 1999; Jackson *et al.* 2002) which accommodate the underthrusting of the South Caspian basement beneath the Talesh Mountains (Fig. 2). No strike-slip fault mechanism parallel with the trend of the southern Talesh has ever been observed, but other geological and geophysical evidence have demonstrated the existence of a significant right-lateral shear in the Eastern Kura Depression in Azerbaijan and the Talesh Mountains further south (e.g. Jackson *et al.* 2002; Allen *et al.* 2003; Kadirov *et al.* 2012). To the north of 39°N, the WCF (Fig. 1) has been proposed along the western boundary of the SCB (e.g. Khain *et al.* 1966; Kaz'min & Verzhbitskii 2011). Based on GPS measurements, the fault has a right-lateral strike-slip component south of the Apsheron Peninsula (Kadirov *et al.* 2012) but its continuation to the south inside the SCB is unclear.

The task of correlating the existing seismicity pattern with active structures in the western SCB is seriously compromised by location biases inherent in single-event location techniques using only regional and teleseismic arrival time observations. The purpose of this study is to reveal more details of the seismicity patterns along the
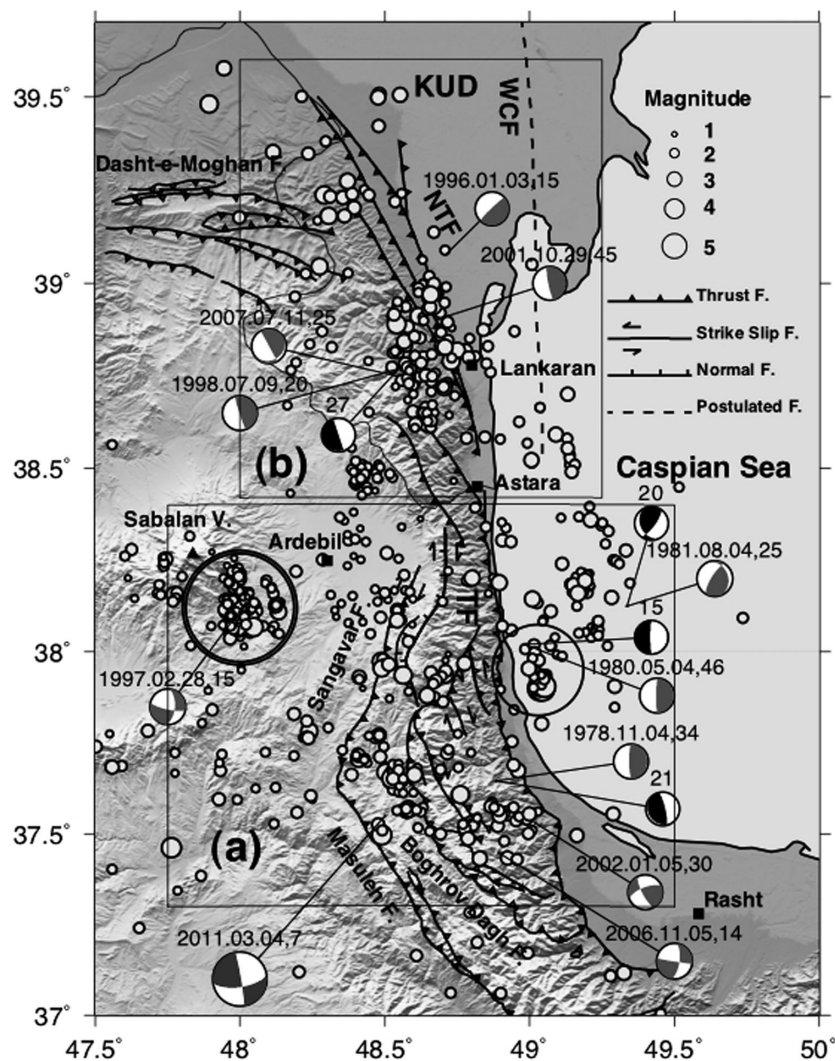
Figure 2. Seismotectonic map of the study region. All of the events shown here were recorded 2009 October 11 through 2011 December 30 by the IASBS temporary network and located with a single-event location technique. Local magnitudes were calculated from the Hutton & Boore (1987) formula. The bold black circle southwest of the Sabalan volcano marks a cluster of events belonging to the Golestan-Ardebil earthquake (1997 February 28, $M_W = 6.1$). The thin black circle marks a cluster of events belonging to the Hashtpar-Gilan earthquake (2010 October 22, $M_L = 5$) and its aftershocks. Grey beachballs are the double-couple part of the global CMT solutions for ten events in the region. Next to each ball, the event date and depth is shown. For four of these events focal mechanisms and depths determined by Jackson *et al.* (2002) is also shown (black beachballs). The large beachball on the Masuleh Fault is the moment tensor solution of the 2011 March 04 ($M_L = 4.2$) event determined by this study. Rectangular boxes (a) and (b) are the southern and northern seismic clusters, respectively, used for the HDC relocation procedure.

western coast of SCB and the bordering Talesh range and understand them in the context of crustal structure and active deformation of the region. We have located as many events as possible by gathering all available phase arrival times from our local temporary network, consisting of an array of seismographs stretching from Astara on the western shoreline of the Caspian Sea to Lake Oroumiyeh near the Iran-Turkey border (Fig. 3), and adding to them data from permanent regional seismic stations, and worldwide networks. Fig. 2 shows the seismicity as recorded by our temporary network. We have used a multiple-event location procedure to obtain calibrated epicentres with absolute location errors less than 5 km. For a subset of events we determined focal depths using near-source crustal arrivals or relative teleseismic depth phases. In addition, we present one new moment tensor solution obtained from regional waveform modelling. We have attempted to shed light on several aspects of deformation of the SCB on its western margin, namely; (1) is there

any offshore seismicity in the western SCB? (2) to what extent has the basement of the South Caspian underthrusted the Talesh Mountains? (3) is the sediment cover involved in seismic faulting? (4) can the right-lateral shear as seen in GPS measurements be inferred from seismicity? and (5) how does the pattern of seismicity change in the transition from SCB to the Talesh Mountains?

The Caspian Sea basin constitutes one of the major petroleum provinces of the world. The hydrocarbon reservoirs in the Caspian Sea are associated with very young structures in the basin and some of them are suggested to be in close connection with active basement faults (Devlin *et al.* 1999). This study provides an improved understanding of the deformational style and basement-controlled seismogenic faulting in the Caspian Basin that can be relevant to hydrocarbon exploration. This study also helps to revise the seismotectonic map of the area, which is of critical value for preparation of seismic hazard maps.
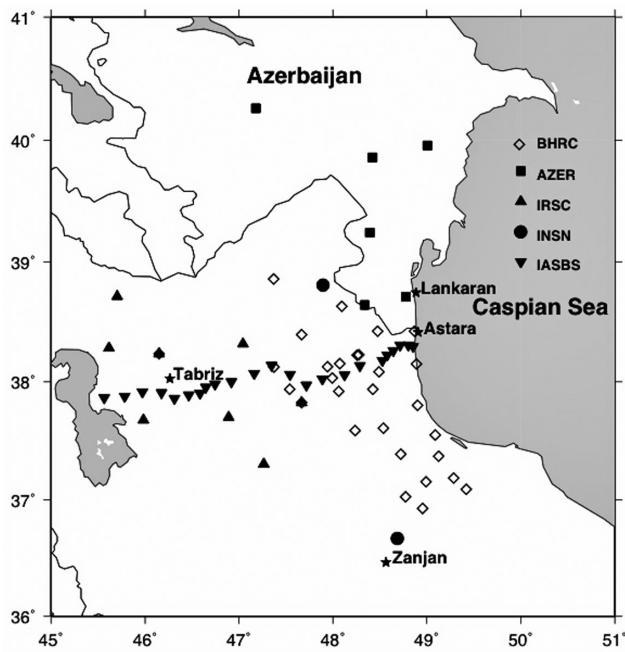
Figure 3. Seismic stations in the vicinity of the study area. The inverted triangles show the IASBS temporary seismic network. Other stations belong to the Iranian National Seismograph Network (INSN), the Iranian Seismological Center (IRSC), the national Iranian accelerometer network (BHRC network) and the Azerbaijan network (AZER).

TECTONIC SETTINGS

The study area covers the southwest shoreline of the Caspian Sea and the Talesh Mountains to the west (Fig. 2). The present-day structural deformation of this region is highly affected by forces related to the Arabia-Eurasia continental collision, and the rheological nature of the SCB. The SCB is a relatively aseismic block and is thought to be a relict backarc basin of the Tethyan Mesozoic arc (e.g. Berberian 1983; Brunet *et al.* 2003; Kaz'min & Verzhbitskii 2011). It is generally agreed that the SCB is subducting beneath the Apsheron-Balkhan Sill which bounds it on the north (Jackson *et al.* 2002; Allen *et al.* 2003; Brunet *et al.* 2003; Knapp *et al.* 2004; Kadirov *et al.* 2012). The crystalline basement of the basin is unusually thick and is much like oceanic crust (Mangino & Priestley 1998; Knapp *et al.* 2004).

Mangino & Priestley (1998) studied the crustal structure of the basin in some detail with the help of receiver function analysis and data from the Deep Seismic Sounding Program of the Soviet Union; Beneath the easternmost Kura Depression in southeast Azerbaijan, the crust is about 50 km, but thinning rapidly to 35 km over a distance of 100 km to the east, into the Caspian. Beneath Lankaran, near the coastline, the thickness of the sedimentary layer is about 15 km, overlying a basaltic layer ($V_p \sim 6.4$–$7\,km\,s^{-1}$) with a thickness of 20 km. In the Kura Depression the crust possesses a midcrustal granitic layer ($V_p \sim 5.8$–$6.4\,km\,s^{-1}$), whereas in the Caspian Basin this layer is absent and the sedimentary cover there sits directly on top of the basaltic layer. Allen *et al.* (2003) show, through an interpreted cross-section, that in northern Talesh the Caspian basement slab must be underthrusting a thinned continental crust 20–25 km thick.

The SCB is surrounded by the arcuate fold and thrust belts of the Talesh, Alborz and Kopeh Dag, which have undergone intense late-Cenozoic crustal shortening. In the west, the southwestward motion of the SCB relative to NW Iran is believed to have resulted

in its underthrusting beneath the Talesh Mountains. But, the extent of the underthrusting is a matter of serious debate as the geological and seismological investigations carried out in the region so far remain inconclusive. The SCB is one of the thickest sedimentary basins in the world, covered by about 20 km thick Cenozoic and older sedimentary sequences (Brunet *et al.* 2003; Knapp *et al.* 2004; Kaz'min & Verzhbitskii 2011). Most of these layers are post-Oligocene in age and their upper parts have been subject to pervasive post-depositional folding which runs subparallel to the shorelines of the basin (Fig. 1). The sedimentary cover contains an overpressured mud-prone layer (the Mykop Series), which probably acts as a decollement horizon separating the surface folding from the deeper basement faulting (Jackson *et al.* 2002).

The southwestern margin of the SCB and the Talesh Mountains are seismically active regions (Fig. 2). Very few focal depths are available and the accuracy of most of the reported locations in global catalogues is suspect, because there are no seismic stations in the immediate area. Locations estimated using regional and teleseismic observations are usually biased by the effect of unknown departures of the assumed theoretical traveltime model from the true velocity structure. Studies of earthquake locations in other parts of Iran that have used specialized procedures to determine bias-free locations find that standard catalogue locations in the region are typically uncertain by 20 km or more (Engdahl *et al.* 2006; Walker *et al.* 2011, 2013). The last major study in the region was that of Jackson *et al.* (2002), who provided focal mechanisms for four events very close to the coastline. These events are 15 to 27 km deep, and all are consistent with low-angle thrust faulting dipping west. These events are most probably associated with faulting in the basement of the SCB (Jackson *et al.* 2002; Engdahl *et al.* 2006), and there is no evidence for seismic deformation of the sedimentary cover of the basin. The observed offshore seismicity does not have sufficient location accuracy to confirm the existence of N–S trending faults that have been inferred to exist in the SCB basement. Based on various geophysical and structural evidence, some authors (e.g. Khain *et al.* 1966; Allen *et al.* 2003; Kadirov *et al.* 2012) have proposed a N–S trending line called the WCF running under the eastern Kura Depression and the western side of the Caspian Sea. Whether this fault continues further south along the Iranian part of the coastline cannot be confirmed from the seismicity in Fig. 2. Nevertheless several clusters of offshore events in Fig. 2 indicate the existence of some N–S trending faults, probably unrelated to WCF.

Recent GPS results (Djamour *et al.* 2010) show the SCB to be in clockwise rotation relative to Eurasia, with a pole of rotation in close proximity to it, resulting in a very tight rotation. Jackson *et al.* (2002) estimated the present day motion of the SCB to be 13–17 mm yr^{-1} to the southwest relative to Iran. This estimate instead used a pole of rotation very far away (about 90 degrees) from the SCB. Other geological investigations have concluded that there must be right-lateral shear motion, in some manner, along the central and southern Talesh Mountains (e.g. Jackson *et al.* 2002; Allen *et al.* 2003; Kaz'min & Verzhbitskii 2011) to accommodate part of the broader Arabia-Eurasia convergence, although detailed and conclusive fieldwork has not been carried out so far. Nevertheless, no earthquake focal mechanism indicative of right-lateral motion has ever been determined in the Talesh.

The Talesh Mountains consist of southern and northern structural arcs that are linked by a central N–S trending segment (Fig. 2). The shape of the southern structural arc is due to the wrapping of the weaker Talesh and Alborz around the more rigid Caspian block. The northern arc takes its shape from a combination of westward motion
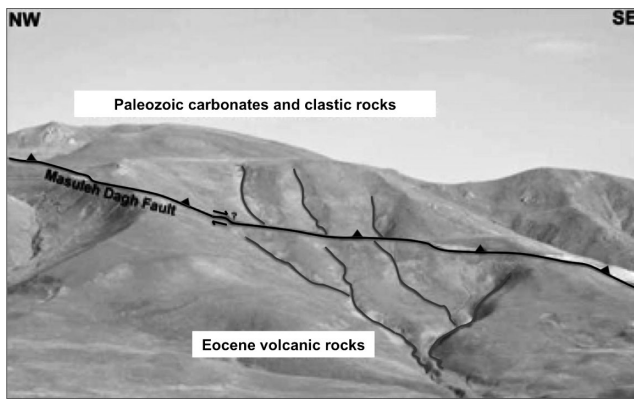
Figure 4. Photograph of the Masuleh Fault zone (location: 37.37°N, 48.59°E). The fault is thrusting the Paleozoic carbonate and clastic rock units over Eocene volcanics at this section. The drainage offsets show the active right-lateral strike-slip kinematics along the fault.

of the SCB and the NE–SW orientation of regional convergence. Therefore, the two arcuate regions are undergoing more intense deformation than the central region. In the central region, the range is made up of N–S folds and thrusts that swing E–W in the northern end of the range. At the eastern edge, the west-dipping Talesh Fault has made a topographic boundary with the SCB (e.g. Berberian & Yeats 1999). The NE-dipping Masuleh and Boghrov Dagh Faults have been introduced as the main active structures in the southern and central parts of the Talesh (e.g. Davies *et al.* 1972; Berberian & Yeats 1999). The right-lateral northern branch of the Masuleh Fault is known as the Sangavar Fault (Berberian & Yeats 1999). Fig. 4 shows a field photograph of the Masuleh Fault where it has thrust the Paleozoic carbonate and clastic rock units over Eocene volcanics. The drainage offsets suggest active right-lateral strike-slip kinematics. The Boghrov Dagh Fault is composed of several hanging wall and footwall strands and extends more than 120 km throughout the Talesh Mountains (Davies *et al.* 1972; Berberian & Yeats 1999). Due mostly to highly vegetative cover and erodible rock units there is little evidence for the style of recent activity of the Boghrov Dagh Fault.

DATA AND NETWORKS

The data for this study come from a temporary seismic network in northwestern Iran installed and operated by the Institute for Advanced Studies in Basic Sciences (hereafter, called the IASBS network) from 2008 August to 2012 July (Fig. 3). The network was a linear array of 23 broadband (100 Hz–120 s) and intermediate-band (50 Hz-120 s) instruments (Table 1) that extended from the western shoreline of the Caspian Sea (Astara) to the eastern side of Lake Oroumiyeh. The network had several research purposes and was not specifically designed for monitoring seismicity. The instruments were CMG-3ESP and CMG-3TD 3-component Guralp Systems and 24-bit DM24 digitizers. Stations were repositioned during the deployment and the recording span at individual sites varied between 12 and 26 months. The instruments recorded in continuous mode with sampling rates of 50 or 100 Hz. The average interstation distance was 13 km.

The linear geometry of the network delivers poor azimuthal coverage for most of the events we have located. Therefore, we included bulletin data from the Iranian Seismological Center (IRSC, irsc.ut.ac.ir) and phase arrival times picked by ourselves from recordings of the Iranian National Seismograph Network (INSN,

www.iiees.ac.ir). More detailed explanations about these networks can be found in Ghods & Sobouti (2005) and Ghods *et al.* (2012). We also used arrival time data from the International Seismological Center (ISC) and the EHB catalogue for Iran (Engdahl *et al.* 1998). The ISC bulletin included phase picks from the nearby Azerbaijan Seismic Network (AZER) that considerably improved the azimuthal coverage at near distances, and thus the location capability of our temporary network. Fig. 3 shows the distribution of seismic stations in the vicinity of the study area. In addition, for relatively large events we considered differential times of S_g–P_g phases from the Iranian Building and Housing Research Center (BHRC) network of digital accelerometers. The BHRC network recorded two of the three largest aftershocks of the Hashtpar Gilan Earthquake (2010 October 22, $M_L = 5$) and 27 other events at very short epicentral distances. The accelerometers do not have calibrated timing, so we could not use absolute arrival times picked from their records.

By combining the data from the IASBS network with these other networks, we have improved the azimuthal coverage and decreased the possibility of systematic location biases caused by deviations of the assumed traveltime model from the true Earth. We further reduced location errors by applying a multiple event relocation technique, which we will discuss below. The IASBS network provides phase readings at very close epicentral distances that play an integral role in the effectiveness of our relocation procedure and substantially reduces the size of location error ellipses.

SINGLE EVENT LOCATIONS

In the first stage of location analysis, a total of 600 events from 2009 October 1 to 2011 December 30 were located using the HYPOCEN-TRE programme (Lienert & Havskov 1995). The result of single-event location is shown in Fig. 2. We picked direct P and S arrival times using the SEISAN software (Havskov & Otemoller 1999). The data used in single-event locations consisted primarily of P_g and S_g readings from the IASBS network and two stations of the INSN. We used a 1-D velocity model routinely used by INSN for locating local and regional events in Iran (Table 2). The depth of the Moho has no effect on our single event location because we used only direct P and S phases. As we will show later, we modified the earth model used for calculating theoretical traveltimes during the process of multiple-event relocation, in which many Pn and Sn arrivals are included. The minimum magnitude of completeness of the IASBS network is about 1.8. Referring to Fig. 2, seismicity is denser in the northern and southern terminations of the Talesh Mountains where the active tectonic trends change. We also observed considerable offshore seismicity along the western margin of the SCB.

MULTIPLE-EVENT RELOCATION

In the second stage of relocations, we applied a multiple-event relocation analysis to two clusters of events in the region. (See Fig. 2 for the location of the clusters.) Our multiple-relocation method is based on the hypocentroidal decomposition (HDC) algorithm of Jordan & Sverdrup (1981), which has been extensively developed by one of us (Bergman) for research in calibrated earthquake location. The method has been applied in a number of recent studies in Iran and elsewhere (e.g. Walker *et al.* 2005, 2011; Biggs *et al.* 2006; Parsons *et al.* 2006; Tatar *et al.* 2007; Bondar *et al.* 2008; Ghods *et al.* 2012).

Table 1. Specification of stations of IASBS temporary seismic network installed in NW of Iran. I.B. and B.B. stand for the intermediate-band and broadband stations, respectively.
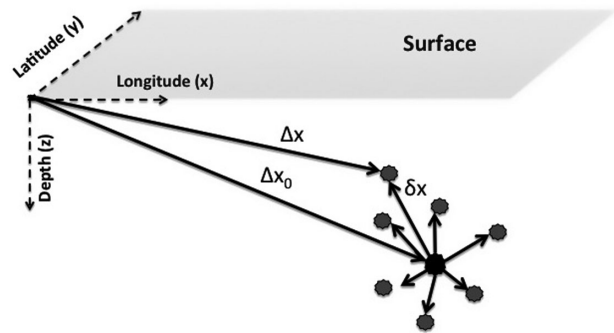
Station	Latitude (degree)	Longitude (degree)	Elevation (m)	Type	Sampling rate (sps)	Recording span
LVND	48.8540	48.8540	58	I.B.	50	2008/09–2010/10
KUTE	48.8038	38.3046	116	B.B.	50	2010/06–2012/04
BALI	48.7161	38.3055	845	I.B.	50	2008/09–2010/06
SOHA	48.6437	38.2601	1400	I.B.	50	2008/08–2010/10
IRIL	48.5781	38.2236	1393	B.B.	50	2010/06–2011/10
IVRI	48.5280	38.1782	1399	B.B.	50	2009/09–2012/04
ZARD	48.2869	38.1353	1560	B.B.	50	2009/10–2010/10
DEIM	48.1256	38.0574	1619	B.B.	50	2009/09–2012/04
BALK	47.8890	38.0215	2060	B.B.	50	2009/10–2010/10
SORK	47.7177	37.9700	1853	B.B.	100	2009/11–2011/10
MIRK	47.5437	38.0588	2055	B.B.	100	2009/11–2011/02
BOLA	47.3474	38.1363	2106	B.B.	100	2009/11–2012/01
SHAD	47.1636	38.0673	1645	B.B.	100	2009/11–2010/10
SEGI	46.9213	37.9993	1649	B.B.	100	2010/06–2011/05
ALVA	46.7450	37.9802	1667	B.B.	50	2010/06–2012/04
SHEB	46.6464	37.9532	1997	B.B.	50	2010/02–2012/04
IRAN	46.5858	37.9020	2055	B.B.	50	2010/02–2011/08
BIRG	46.4670	37.8863	2060	B.B.	50	2010/02–2011/10
A000	46.3145	37.8583	2137	B.B.	100	2010/12–2012/06
ESFN	46.1748	37.9063	1647	B.B.	100	2010/12–2012/01
BEIG	45.9737	37.9134	1377	B.B.	100	2010/11–2011/10
KHOR	45.7842	37.8760	1292	I.B.	50	2010/12–2012/06
SARA	45.5654	37.8634	1318	I.B.	50	2010/12–2012/06

Table 2. The crustal model (Tatar 2001; Doloei & Roberts 2003; Kaviani 2004) used in single-event earthquake location in Iran. A V_P/V_S ratio of 1.73 was used to derive the S velocities.

Layer	p velocity (km s^{-1})	Depth to top of layer (km)
1	5.4	0
2	6.0	6
3	6.3	14
4	6.5	18
5	8.05	51
6	8.1	80

Figure 5. Illustration of the HDC method. The hypocentroid (black circle) is the geometrical average of cluster members (grey circles) and Δx_0 is the displacement vector of this virtual point. Cluster vector, δx, is the location of an event in the cluster relative to the hypocentroid. The displacement vector of an event, Δx, is the sum of Δx_0 and δx.

All multiple-event relocation methods are based on reducing location error due to the correlation of traveltime errors along similar paths. Ray paths arriving from a distant, closely cluster group of earthquakes at a specific seismic station, sample nearly the same portion of the Earth once outside the immediate source volume. Therefore, much of the error (theoretical minus observed traveltime) at a given station for those readings is correlated. The correlated error can be removed to a large extent by working with arrival time differences (same phase, recorded at a common station) rather than absolute traveltimes, thus improving resolution of relative locations.

The advantage of the improved HDC method over other established methods such as the double-difference and the joint hypocentroidal decomposition (JHD), is in its flexibility to add different kinds of data to locate a given cluster. We used simultaneously local, regional and teleseismic absolute and relative phases in our analysis. Another advantage of the HDC method is its ability to manage large volume of data from large number of stations. The input for the double difference method is the time difference of arrival times of all hypocentral pairs for different stations which are much larger in number than those used in HDC. The HDC uses arrival time difference of different events relative to the hypocentriod of the cluster for its relative relocation. In the JHD method, station corrections are entered into the analysis as variables, which makes

it an unattractive method when working with large volumes of data from a large number of stations. In the HDC method calculation of station corrections is not requires.

The HDC method is unique among multiple-event relocation methods in separating the location problem of a cluster of events into two parts, the relative locations of all events (known as cluster vectors) with respect to a reference point (the hypocentroid) in space and time, followed by the estimation of the location of the hypocentroid in absolute coordinates, which establishes the absolute locations of all events in the cluster by adding the cluster vectors to the hypocentroid (Fig. 5). The hypocentres calculated from single-event location procedure are used as initial locations for the multiple-event analysis. The data set of arrival times can be, and usually should be, different for the two estimation procedures, and the error terms that need to be considered are different as well. For example, it is not necessary to include the uncertainty in theoretical traveltimes in the estimation of the cluster vectors (because only traveltime differences are used), but this is a significant factor

in the estimation of the hypocentroid. Furthermore, we can estimate the hypocentroid using only data at short distances, drawing on all such data from every event in a cluster, and thus minimize the biasing effect of unknown velocity structure. We may use all types of phase readings coming from all epicentral distances to calculate the cluster vectors because the bias caused by unmodelled earth structure is largely removed by taking traveltime differences. The ability to tailor the data set and error terms specifically to the two estimation procedures is the reason that HDC is especially suited to relocation studies where location accuracy is at a premium, as well as the reliable estimation of the uncertainty in location.

The error in the location of each event relative to the hypocentroid (cluster vector) describes only a portion of the total uncertainty in location. In seismotectonic analyses, where one wishes to match seismicity with the causative faults, the relative location error between clustered events can be extremely useful, but the total uncertainty in location for any event must also include the uncertainty in the hypocentroid. The factors controlling location error of the hypocentroid are the same as those that determine the accuracy of single-event location: number of readings, completeness of azimuthal coverage, having direct P and S phase readings at near distances, size of uncertainties of the arrival time picks, and appropriateness of the assumed traveltime model. To minimize the location error of the hypocentroid, we used only P_g, S_g and S_g–P_g phase readings of the cluster at small epicentral distances. Although few events in the cluster have enough readings at short distances with good azimuthal distribution to yield highly accurate locations by themselves, when all such data are combined for estimation of the hypocentroid of the cluster, the quality of the data set can be remarkably good.

In the HDC analysis changes in cluster vectors (from starting locations determined in single-event analysis) are calculated first, after which an improved hypocentroid is calculated, based on the revised relative locations. The programme repeats this two-step process to convergence, usually in 2–4 iterations.

This process is repeated many times as we progressively identify and remove outlier readings from the arrival time data set after each run. This 'cleaning' process is essential in order to finally obtain estimates of location and location uncertainty that are consistent with the statistical nature of the data set. It is based on the fact that we have multiple samples of the traveltime of a specific phase from a limited source region to a specific recording site. Analysis of the residuals of these observations provides an estimate of the spread of residuals as well as their mean departure from the theoretical traveltime model. Because the residual distribution is, in general, contaminated by outliers, it is crucial to use a robust estimator of spread (Croux & Rousseeuw 1992). Outliers are identified by their distance from the mean of residuals for that station-phase, normalized by the spread, which we call 'empirical reading error'. Clearly, it includes contributions from error sources other than pure reading error. The cleaning process is done progressively, eliminating the largest outliers first, until the data set is judged to be statistically consistent with the empirical reading errors. In practice this means trimming until there are no readings with residuals greater than 3 sigma.

Each of the two clusters we have analysed here is composed of events recorded by our temporary network, as well as a number of older events listed in the EHB catalogue for the period 1980–2008 (Engdahl *et al*. 1998). Tables 3 and 4 give a list of events of these clusters. By bringing the older EHB data into the clusters and improving their location accuracy, we manage to have a reliable seismicity data that spans 30 yr. This gives us a power of geological interpretation that would not be possible with the 2 yr data of the temporary network alone. The southern cluster (box a), includes 114 events in the southern Talesh and offshore of it, and the northern cluster (box b) in southernmost Azerbaijan has 41 events. Events having a local magnitude larger than 2.5, a minimum number of 12 readings, and an azimuthal gap smaller than 220° were included in the clusters. We took an expanded area for the southern cluster to include the events in western Talesh in order to have more data for a statistical analysis of the readings. A large number of readings is desirable for carrying out more efficiently the 'cleaning' process which involves identifying and flagging outlier readings in the arrival time data set, to improve the estimation of the empirical reading errors (below). We found that adding well-located events outside of the Talesh Mountains, especially a cluster of events belonging to the Golestan-Ardebil earthquake (1997/02/28, $M_w = 6.1$) (the black circle in Fig. 2), offsets the probability of biases introduced by heterogeneity in the velocity structure of the expanded region, which contains the SCB as well as more 'typical' continental regions. The selected events from Golestan-Ardebil cluster are well recorded with the help of the nearby BHRC accelerometer stations.

We initially fixed focal depths for both clusters analysed here because we did not have enough depth phases or readings from very close stations to constrain the depth of all events in the clusters. The fixed values were based on the well-constrained events and/or geological considerations. After cleaning the data sets, we manually estimated the depth for those events that either had one or more direct phase readings at short epicentral distances or those with several relative depth phases (i.e. pP-P and sP-P). We are unable to use depth phases in a direct sense because the P branch (and thus, the depth phase branches as well) of the ak135 traveltime model used for teleseismic phases has a significant baseline offset from the calibrated origin times. We estimated focal depths only for events with large number of pP-P and/or sP-P readings. This allows us to use a statistical approach to remove serious outliers from the set of pP-P and sP-P readings. The depths calculated from readings at short epicentral distances are in close agreement (usually within a few km) with those calculated from relative depth phases.

The southern cluster

The majority of the events in the southern cluster (66 out of 114 events) were chosen from the data recorded by the IASBS network with local magnitude larger than 2.5. The remaining 48 were extracted from the EHB catalogue for the period 1980–2008. The default depth of the cluster was fixed at 14 km based on the average depth calculated for onshore events at close proximity to stations. The events have a minimum number of 12 readings, open azimuth smaller than 220° (for 23 events open azimuth is smaller than 50°, for 68 it is between 50° and 150°, and for 23 it is between 150° and 220°). Eleven of the events are associated with the Hashtpar earthquake ($M_L = 5$), the largest located event in the time span considered. The cleaned data set contains 5671 readings and 1013 independent station-phases to estimate the cluster vectors (342 free parameters). The number of 'short distance' readings was rather large and well-enough distributed (Fig. 6a) to allow for directly locating the hypocentroid using only these data. We estimated the location of the hypocentroid using 1429 arrival times, all for distances less than 1.7° (Figs 6a and 7a) and with 118 independent station-phase pairs. The arrival times of P_g and S_g in this distance range are fit very well with a two-layered crustal model. The lengths of the semi-axes of the 90 per cent confidence ellipse of the

Table 3. Statistics for the relocated events in the southern cluster using the HDC method. In determining the epicentral coordinates, only local distance data was used to locate the hypocentroid and calibrate the cluster. Magnitudes for larger events are from the ISC. For smaller events, we calculated local magnitude (M_L) using the Hutton & Boore (1987) relationship. The 90 per cent confidence ellipses for absolute location (summing uncertainties in the cluster vectors and the hypocentroid) are given in columns 12–16: AZ1 and AZ2 are azimuths of elliptical semi-axes, and L1 and L2 are the corresponding semi-axis lengths in km. The Area column gives the area of the confidence ellipse in km^2. The last column reports the depth of the events estimated by this study; Depths estimated by S-P readings of BHRC stations or the absolute P arrival times of near stations are marked with the '‡' symbol (reported in Fig. 10a); depths estimated by secondary depth phases are marked with the '†' symbol (reported in Fig. 10b); depths of events marked with no symbol are fixed to a default value.

Event number	Year	Month	Day	Hour	Minute	Second	Lat.	Long.	Mag.	Type	AZ1	AZ2	L1	L2	Area	Depth
1	1970	7	11	22	41	11.77	37.53	49.02	5.2	Mb	38	278	1.8	2.7	15	25†
2	1971	5	15	4	53	3.85	37.82	48.97	4.7	Mb	67.8	274	2	2.8	18	14
3	1972	1	18	21	12	1.6	37.48	48.97	4.8	Mb	81.2	306	2.6	5.5	46	14
4	1978	11	4	15	22	18.8	37.65	48.89	6	Mb	47.3	279	1.2	1.8	7	26†
5	1979	8	27	16	9	48.53	37.81	49.05	4.6	Mb	131.3	301	3.1	6.1	59	14
6	1979	9	7	22	53	55.77	37.48	49.01	4.7	Mb	190.5	13	1.3	4	16	14
7	1980	5	4	18	35	18.34	38.02	48.98	5.3	Mb	21.8	278	1.1	1.6	6	22†
8	1980	5	5	10	21	47.27	38.04	49.04	4.6	Mb	87.4	286	1.6	2.9	15	14
9	1981	8	4	18	35	41.03	38.12	49.34	5.4	Mb	35.2	276	1.2	1.9	7	18†
10	1984	9	30	15	33	17.8	37.83	49.03	4.6	Mb	65.1	293	2	4	26	14
11	1985	4	3	1	44	24.76	37.84	48.32	4.7	Mb	69.8	289	1.5	3.4	16	9†
12	1986	4	29	22	7	54.34	37.86	48.99	4.9	Mb	67.1	288	1.4	2.7	12	23†
13	1986	4	29	23	35	38.48	37.62	48.87	4.3	Mb	195.9	302	1.7	2.3	12	14
14	1990	9	24	6	35	13.51	38.05	47.95	4.6	Mb	97.1	283	2	3.3	20	10†
15	1994	11	2	12	31	2.48	38.1	48.11	4.7	Mb	102	279	1.5	2.7	13	16‡
16	1994	12	3	1	35	48.8	37.38	49.2	4.6	Mb	77.8	292	2.2	4.3	29	14
17	1996	5	28	22	18	28.97	37.67	48.77	3.9	Mb	83.5	322	3.7	4.3	49	14
18	1997	2	28	12	57	20.45	38.11	48.01	5.5	Mb	35.6	274	1.2	1.7	6	15‡
19	1997	2	28	13	56	0.51	38.11	47.98	4.2	Mb	116.5	24	1.5	3.6	17	16‡
20	1997	2	28	20	55	11.38	38.04	47.9	3.8	Mb	56.1	64	1.5	1.6	8	12‡
21	1997	2	28	21	46	22.05	38.12	47.9	3.8	Mb	38.1	9	1.7	1.7	9	18‡
22	1997	3	2	18	29	43.73	38.05	47.95	5	Mb	31	282	1	1.2	4	10‡
23	1997	3	21	23	0	41.23	38.07	47.95	4.4	Mb	36.1	71	1.3	1.5	6	14‡
24	1997	4	1	7	33	27.97	37.93	49.1	3.5	Mb	119.9	298	1.2	3.2	12	21†
25	1997	4	8	5	44	14.82	38.02	47.95	3.6	Mb	76.8	295	1.4	2.2	10	10‡
26	1997	4	20	18	4	28.93	37.99	47.92	3.7	Mb	70.4	282	1.5	2.3	11	12‡
27	1997	5	12	3	51	1.44	37.99	47.96	4.6	Mb	43	292	1.3	1.5	6	10‡
28	1997	8	24	11	48	12.71	37.55	48.85	4.2	Mb	202.4	273	2.3	6.8	50	14
29	1997	10	17	21	14	5.13	38.1	47.95	3.8	Mb	81.4	289	1.1	1.6	6	14
30	2000	1	28	3	29	16.06	37.81	49.15	4	Mb	77	313	1.6	2.8	14	14
31	2000	4	10	3	42	39.22	38.1	48	3.9	Mb	37.3	73	1.5	1.9	9	12‡
32	2000	5	19	5	31	15.86	38.11	47.99	3.6	Mb	66.2	87	1.6	2.5	12	14‡
33	2000	9	5	15	1	31.89	37.45	48.5	4	Mb	160.1	298	1.1	3	11	14
34	2002	1	5	14	43	44.12	37.53	49.02	4.4	Mb	23	306	1.2	1.9	7	23‡
35	2002	1	6	6	22	25.91	38.23	48.95	4.2	Mb	39.8	300	1.2	2.4	9	37‡
36	2003	5	2	8	9	52.5	37.37	49.05	3.8	Mb	86.7	299	1.5	2.6	12	10†
37	2003	10	16	10	56	48.95	38.06	47.98	3.7	ML	130.9	296	1.2	3.2	12	12‡
38	2004	12	19	21	27	57.46	38.08	48.41	3	ML	118.3	301	3.2	5.7	58	14
39	2005	8	27	7	18	5.21	37.83	48.49	3	ML	130.9	284	1.6	2.3	11	14
40	2005	12	20	4	47	29.11	37.94	49.02	3.7	ML	90.4	286	2.1	4	26	14
41	2006	1	13	4	57	16.67	38.12	47.97	3.4	Mb	96.2	321	2	2.5	15	11‡
42	2006	9	14	19	54	56.84	37.51	48.96	3.2	Mb	62.3	299	1.9	2.8	16	14
43	2006	11	5	20	6	41.12	37.45	48.89	4.7	Mb	28	294	1.1	1.5	5	23‡
44	2006	12	11	14	46	16.64	37.64	49.29	3.6	ML	153.7	299	1.8	3.3	18	14
45	2007	8	20	16	8	58.66	37.49	49.09	4	Mb	110	303	1.4	2.2	10	28‡
46	2007	12	6	20	30	54.28	37.53	48.62	3.5	ML	159.3	301	1.9	3.8	23	14
47	2008	7	13	22	30	7.48	37.67	48.18	4.3	Mb	123.8	302	1.2	2.2	8	9‡
48	2008	12	26	1	48	13.06	38.07	49.21	2.8	ML	177.1	79	2.1	3.9	26	14
49	2009	10	14	16	11	48.61	37.95	48.7	3.2	ML	110.7	25	1	1.1	3	14
50	2009	10	27	10	28	14.5	37.44	48.95	2.7	ML	200.9	356	1.1	3.1	11	14
51	2009	11	10	18	52	30.65	37.95	48.71	2.6	ML	161.7	51	0.9	1.4	4	14
52	2009	11	27	1	26	4.7	37.69	48.97	2.9	ML	125.3	67	1.2	1.3	5	14
53	2010	1	16	1	27	16.79	37.53	48.47	4.1	ML	82.1	21	0.9	1	3	9‡
54	2010	1	16	2	3	4.74	37.53	48.5	2.5	ML	130.8	65	1.4	2	9	14
55	2010	2	18	14	33	8.91	38.11	48.53	2.7	ML	86.5	63	0.8	2	5	11‡
56	2010	2	20	6	49	10.24	37.58	48.97	2.9	ML	201.1	354	1.1	1.5	5	12
57	2010	3	10	7	29	40.91	37.57	48.93	2.6	ML	154.7	296	1.6	1.8	9	14
58	2010	3	10	18	2	12	37.55	48.93	2.9	ML	142.2	23	1.2	1.3	5	14
59	2010	5	19	1	49	42.41	38.14	48	2.5	ML	98.3	76	0.8	1.2	3	11‡

Table 3. (*Continued.*)

Event number	Year	Month	Day	Hour	Minute	Second	Lat.	Long.	Mag.	Type	AZ1	AZ2	L1	L2	Area	Depth
60	2010	5	19	2	2	31.24	38.14	48	2.8	ML	98.5	83	0.9	1.2	3	10‡
61	2010	5	29	12	1	15.38	37.68	48.39	2.5	ML	119.9	65	1	1.8	6	14
62	2010	7	8	2	45	56.85	37.95	48.65	2.6	ML	160.2	36	0.8	1	2	14
63	2010	8	2	18	5	4.8	38.14	48.82	3.1	ML	128.3	59	1.7	2.7	14	34‡
64	2010	8	23	21	22	54.49	37.94	48.49	3.7	ML	79.4	50	0.9	1.3	4	9‡
65	2010	8	24	4	11	0.06	37.97	48.47	3.4	ML	112.2	47	0.9	1.3	4	9†
66	2010	8	27	19	58	35.12	37.57	48.57	3.1	ML	108.5	358	1	1.2	4	6‡
67	2010	9	4	7	19	18.55	37.96	48.49	2.7	ML	137.5	47	1.2	1.5	5	9†
68	2010	9	20	13	39	38.48	37.56	48.59	2.6	ML	162.1	10	0.9	1	3	14
69	2010	9	21	14	59	20.56	37.57	48.58	2.8	ML	118	2	0.9	1.4	4	14
70	2010	9	22	18	38	36.58	38.36	49.17	3	ML	274.6	318	2.7	3.5	30	32‡
71	2010	9	24	3	49	27.08	37.85	48.74	3	ML	128.7	70	1.7	1.8	9	14
72	2010	10	22	8	0	38.2	37.94	49.05	5	ML	23.2	273	1.1	1.4	5	26†
73	2010	10	22	8	5	39.29	37.93	49.05	2.7	ML	220.9	353	0.9	1.2	3	14
74	2010	10	22	8	20	34.36	37.93	49.05	2.5	ML	220.4	352	0.9	1.2	3	14
75	2010	10	22	8	20	34.36	37.92	49.05	2.5	ML	220.1	353	0.9	1.2	3	14
76	2010	10	22	8	34	24.09	37.91	49.08	4.9	ML	92.3	293	1	1.2	4	14
77	2010	10	22	8	43	22.22	37.93	49.04	2.5	ML	219.8	349	1.1	1.4	5	14
78	2010	10	22	9	8	26.3	37.94	49.08	4.7	ML	56	277	1	1.2	4	19‡
79	2010	10	22	9	43	9.07	37.94	49.04	3.1	ML	219.2	348	1.1	1.4	5	14
80	2010	10	22	11	36	20.34	37.94	49.05	3.1	ML	221.6	351	1	1.2	4	14
81	2010	10	23	8	24	54.52	37.92	49.05	2.7	ML	220.7	351	1	1.2	4	14
82	2010	10	23	17	19	50.74	37.91	49.09	4.4	ML	79.2	293	1	1.4	4	14
83	2010	10	26	19	45	55.46	38.09	48.51	3	ML	126.4	58	1	2.5	8	9‡
84	2010	11	9	16	51	26.82	38.1	49.05	3.1	ML	166.8	275	1.4	2.2	10	14
85	2010	12	6	8	24	54.36	37.57	48.89	2.5	ML	195.6	352	1	2.5	8	14
86	2010	12	6	21	18	26.67	37.54	48.84	2.9	ML	133	353	1.1	1.5	5	14
87	2010	12	8	17	55	8.1	37.78	48.23	3.3	ML	114.2	71	1	1.2	4	9‡
88	2011	2	23	23	18	42.3	37.72	48.74	2.5	ML	177.9	60	1.7	2.8	15	14
89	2011	3	3	18	22	13.82	37.65	48.5	3.3	ML	78.4	66	1.3	1.5	6	7‡
90	2011	3	4	9	46	27.92	37.65	48.5	4.2	ML	34.5	309	1.5	1.6	8	7‡
91	2011	5	10	13	4	25.16	37.67	48.5	2.6	ML	145.2	74	1.2	1.7	6	14
92	2011	6	16	14	10	46.42	37.81	48.2	2.6	ML	134.7	77	1.2	3.1	12	14
93	2011	6	25	21	35	10.05	37.9	49.02	2.9	ML	214.9	52	1.6	1.8	9	14
94	2011	7	8	8	53	56.11	37.61	48.8	3.5	ML	103.4	300	1.5	1.7	8	14
95	2011	7	9	0	35	8.87	38.2	49.21	3	ML	207.9	327	1.7	2.6	14	37‡
96	2011	7	16	13	1	44.94	37.53	48.81	2.6	ML	156.6	352	1	2.3	8	14
97	2011	7	16	20	58	20.71	38.19	48.96	3.2	ML	235.3	318	2.3	3.3	24	43‡
98	2011	7	24	2	33	19.82	38.09	48.04	3.8	ML	140.7	79	0.9	1.9	5	8‡
99	2011	8	10	6	16	9.45	37.5	49.19	2.7	ML	159.6	351	1	1.7	5	14
100	2011	8	16	5	7	55	38.12	48.12	2.7	ML	85.4	76	0.8	1.4	3	14‡
101	2011	8	16	10	49	54.39	38.14	48.12	2.7	ML	162.2	77	0.8	2.1	5	13‡
102	2011	8	16	18	27	11.21	38.13	48.12	3.1	ML	144.2	76	0.8	1.7	4	13‡
103	2011	8	19	17	48	7.15	38.13	48.12	2.5	ML	163.9	79	0.8	1.8	4	14‡
104	2011	8	28	19	27	23.16	37.72	48.4	3.2	ML	81.7	360	1.2	1.3	5	14
105	2011	8	30	11	47	56.54	37.72	48.41	2.8	ML	103.7	26	0.9	1	3	14
106	2011	9	5	10	34	44.3	37.56	48.95	2.8	ML	202.4	352	1.2	1.9	7	14
107	2011	9	16	11	36	46.89	37.91	48.41	2.7	ML	131.6	64	0.8	1.8	5	14
108	2011	9	19	23	6	17.34	37.86	48.68	3.1	ML	93.8	61	1.1	1.3	4	14
109	2011	9	25	16	17	59.14	37.49	48.79	2.8	ML	185.1	351	1.4	2.2	10	14
110	2011	10	7	11	25	28.43	37.93	48.52	3.6	ML	86.5	41	1.5	1.8	8	9‡
111	2011	10	16	13	57	13.73	37.47	48.91	2.9	ML	143	304	1.9	2.5	15	14
112	2011	10	23	16	35	13.45	37.66	48.59	3.2	ML	118.4	7	1	1.2	4	10‡
113	2011	10	27	8	33	5.64	37.74	49.15	2.8	ML	168.4	69	2	2.4	15	14
114	2011	11	3	21	49	32.34	38.04	49.21	3.1	ML	196.8	338	1.4	2.3	10	14

hypocentroid are 0.6 and 0.8 km and its larger axis has an azimuth of 41°. The final estimates of location errors for the events of the cluster vary from 1 to 6 km, with most being less than 2.5 km. The result of the HDC analysis for the cluster is listed in Table 3.

Fig. 8 shows the relocated epicentres of the southern cluster. Each event is shown with its 90 per cent confidence ellipse for relative relocation. The white ellipses are the relocated events of the EHB catalogue and the grey ones are for the IASBS network. The uncertainties in relative locations are related to the length of the larger semi-axis of the confidence ellipses. The location uncertainties are generally smaller for onshore events because of better azimuthal coverage. Relocated events from the EHB catalogue generally have larger uncertainties compared to those recorded by the IASBS network.

Table 4. Statistics for the relocated events in the northern cluster using the HDC method. For table details see caption of Table 3.

| Event number	Year	Month	Day	Hour	Minute	Second	Lat.	Long.	Mag.	Type	AZ1	AZ2	L1	L2	Area	Depth
1	1970	4	16	1	26	49.77	38.88	48.61	4.6	mb	45.4	271	1.6	2	10	26
2	1970	12	23	17	31	28.21	38.74	48.68	4.0	mb	129.6	308	2.9	4.5	41	26
3	1979	11	8	5	21	59.71	38.74	48.71	4.5	mb	138	84	2.3	2.8	20	26
4	1979	11	23	19	43	31.91	38.88	49.03	4.5	mb	134.6	80	2.4	5.4	40	26
5	1983	4	2	0	32	28.64	39	48.58	4.7	mb	81.4	287	1.3	2.3	9	24‡
6	1985	5	9	18	50	26.95	39.03	48.86	4.4	mb	91.5	287	1.7	2.9	15	26
7	1986	1	27	16	35	50.2	39.03	48.68	5.3	mb	28.5	288	1.1	1.5	5	22†
8	1986	11	5	1	15	35.53	38.94	48.67	4.5	mb	50.6	303	1.7	2	11	26
9	1995	5	27	21	21	32.98	38.99	48.94	4.7	mb	54.1	280	1.2	1.8	7	26
10	1995	8	17	18	9	57.41	38.99	48.79	3.9	mb	91.5	78	1.8	2	12	26
11	1996	1	3	8	42	25.64	39.08	48.71	4.9	mb	70.4	281	1.2	1.9	7	32†
12	1997	2	13	0	47	36.8	38.73	48.87	3.9	mb	59.9	294	1.5	1.8	8	26
13	1998	7	9	14	19	20.77	38.77	48.55	5.8	mb	29.4	289	1.1	1.4	5	27†
14	1999	10	3	13	19	15.35	38.96	48.74	4.3	mb	52.4	284	1.3	1.7	7	26
15	1999	10	12	15	41	15.01	39.14	48.35	4.6	mb	52.5	293	1.2	1.6	6	32†
16	2001	10	29	10	4	49.31	38.9	48.68	4.5	mb	32.1	293	1.1	1.6	6	30†
17	2005	5	26	1	59	7.55	38.68	48.64	4.3	mb	41.5	295	1.3	1.7	7	35†
18	2006	12	2	13	23	53.15	38.81	48.54	4.0	mb	68.5	284	1.3	1.6	6	26
19	2007	7	11	6	51	14.91	38.75	48.54	4.9	mb	22	289	1.1	1.4	5	30‡
20	2007	7	14	12	12	13.13	38.78	48.57	3.7	ML	116.1	298	2	3.1	19	18†
21	2008	6	10	14	54	28.22	39.25	48.9	3.9	mb	54	314	1.3	1.5	6	35†
22	2009	10	17	20	27	54.59	39.16	48.36	2.7	ML	128.6	325	1.4	1.8	8	30‡
23	2009	10	19	3	37	41.05	39.18	48.01	2.6	ML	125	352	2	2.2	14	20‡
24	2009	10	24	0	30	36.95	39.22	48.32	3.5	ML	52.8	18	1.7	1.8	10	14‡
25	2009	12	3	5	12	35.89	38.82	48.74	2.8	ML	111.8	347	1.6	1.9	9	40‡
26	2009	12	30	17	10	14.71	39.31	47.95	2.9	ML	227.3	282	2.3	3.4	25	26
27	2010	1	29	16	33	32.77	38.74	48.57	3.2	ML	86.1	297	1.3	1.4	6	24‡
28	2010	2	6	18	0	18.74	38.89	48.59	3.4	ML	118.2	340	1.5	1.8	8	36‡
29	2010	2	13	12	35	43.73	38.71	48.67	3.1	ML	82.1	339	1.6	1.8	9	22‡
30	2010	6	16	22	35	36.27	38.65	48.94	2.9	ML	174.8	79	1.7	3.8	20	47†
31	2010	9	10	9	49	54.16	38.63	48.61	3.3	ML	61.4	332	1.4	1.5	6	33‡
32	2010	9	10	15	21	41.04	38.65	48.59	2.7	ML	228.2	295	1.4	1.9	8	26
33	2010	10	8	20	58	15.19	38.88	48.5	3.9	ML	94.5	313	1.4	1.6	7	30‡
34	2011	3	11	0	31	57.44	38.96	48.81	2.6	ML	224.2	79	2.6	3.4	28	26
35	2011	4	5	20	3	30.77	38.9	48.64	3.2	ML	118.8	337	1.9	2.3	14	30‡
36	2011	4	26	20	11	37.73	39.33	48.27	3.2	ML	79.1	335	2	2.3	15	26‡
37	2011	5	26	3	21	40.19	38.78	48.7	3.1	ML	127.9	346	2.9	3.7	34	42‡
38	2011	7	12	0	34	31.21	38.86	48.69	3.1	ML	190.1	72	1.7	2.5	14	26
39	2011	8	28	9	43	21.79	38.8	48.54	3.0	ML	108.9	320	1.3	1.5	6	25‡
40	2011	11	3	15	22	43.71	38.91	48.63	3.4	ML	119.1	338	1.6	1.9	10	30‡
41	2012	2	4	6	19	32.51	38.63	48.72	4.2	ML	64.7	76	2.1	2.4	16	26
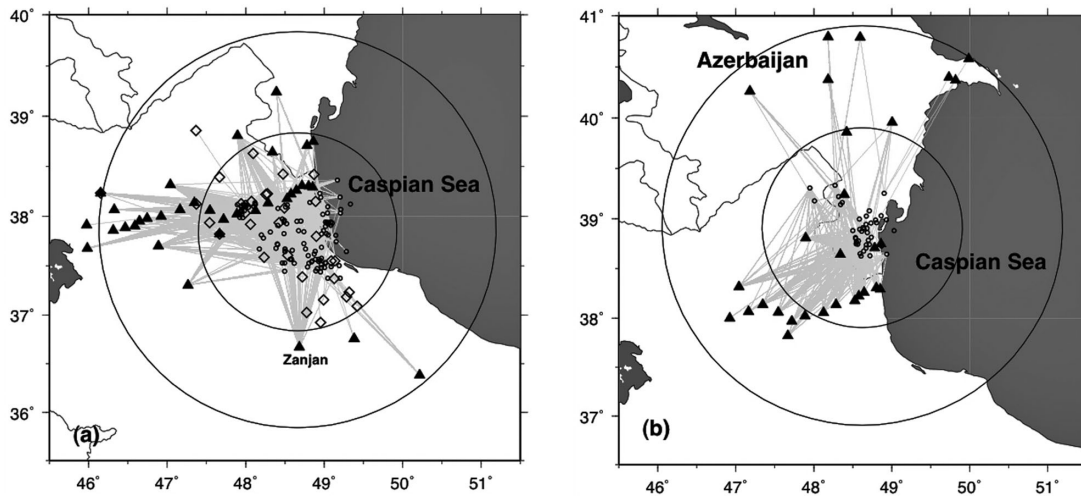
Figure 6. Ray paths used to locate the hypocentroid of the southern (a) and northern (b) clusters. Open circles are cluster events. Solid triangles are stations. Open diamonds are BHRC accelerometer stations. Large circles are centred at the hypocentroids with radii of 1° and 2°.
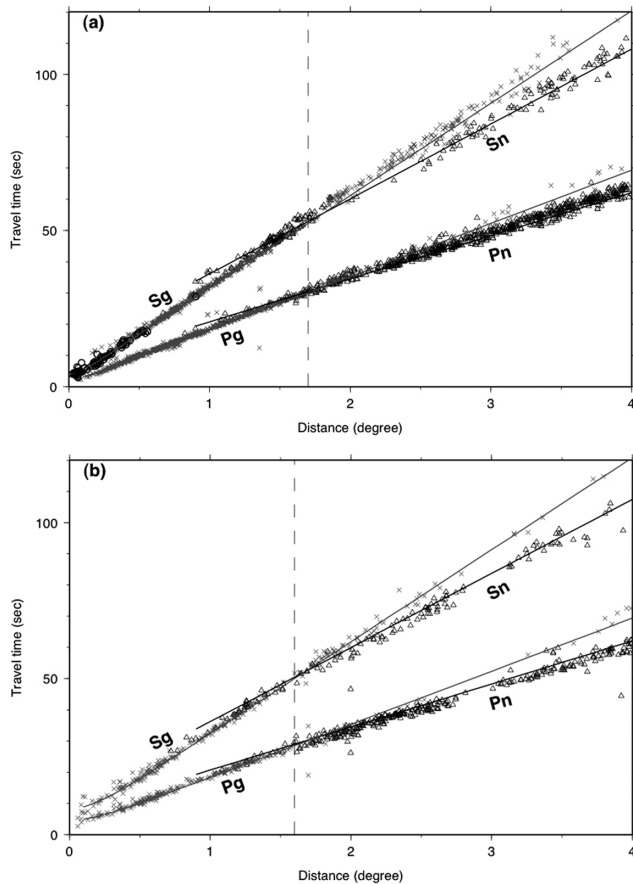
Figure 7. Observed phase arrivals and traveltimes calculated from the local velocity model used for calibrated location of the two clusters. (a) The southern cluster; a two-layer crust (upper layer 15 km, $V_p = 5.9$ and $V_s = 3.35 \, \text{km s}^{-1}$; lower layer 44 km, $V_p = 6.5$ and $V_s = 3.75 \, \text{km s}^{-1}$) over a half-space ($V_p = 8.2$ and $V_s = 4.7 \, \text{km s}^{-1}$) best fits the observed phase arrivals. (b) The northern cluster; a two-layer crust (upper layer 15 km, $V_p = 5.8$ and $V_s = 3.15 \, \text{km s}^{-1}$, lower layer 50 km, $V_p = 6.5$ and $V_s = 3.75 \, \text{km s}^{-1}$) over a half-space ($V_p = 8.0$ and $V_s = 4.65 \, \text{km s}^{-1}$) best fits the observed phase arrivals. The dashed lines show the cut-off distances (1.7° and 1.6°, respectively) for data used for calculation of the hypocentroid. In each plot, the upper graph shows the P traveltime curve (crosses for P_g, triangles for P_n) and the lower graph shows the S traveltime (crosses for S_g and triangles for S_n). Open circles in (a) are S_g–P_g phases derived from the BHRC accelerometer stations which do not have calibrated timing systems. These are plotted by adding the S_g–P_g time to the theoretical P_g arrival time at the corresponding distance. For all phases, theoretical traveltimes (lines) are shown for the average depth of events in each cluster.

The northern cluster

The northern cluster of earthquakes covers the northern part of the Talesh Mountains and contains 41 events, 20 events with magnitudes greater than 2.5 recorded by the IASBS network and 21 from the EHB catalogue for the period 1980–2008. The depth of the cluster was fixed at 26 km based on the average depth estimated for earthquakes with readings at short epicentral distances. The events have a minimum number of 12 readings, open azimuth less than 230° (for 17 events azimuthal gap is less than 50°, for 19 it is between 50° and 150°, and for 5 events it is between 150° and 230°). A total of 2416 readings were used for estimating the cluster vectors (123 free parameters) and the number of independent station-phases was 627. We estimated the location of the hypocentroid of the cluster using 432 arrival times, all for distances of less than 1.6° (Fig. 6b),
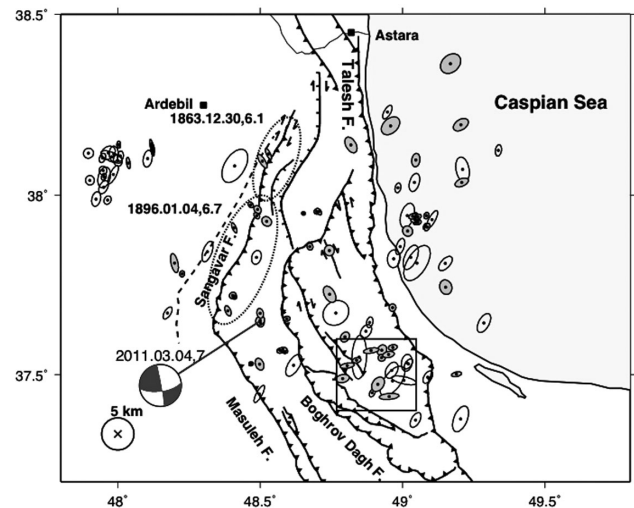
Figure 8. Epicentres of earthquakes in the southern cluster relocated with the HDC analysis. Each location is shown with its 90 per cent confidence ellipse. Open ellipses are for events of the EHB catalogue and grey ellipses are for events recorded by the IASBS network. The beachball is the focal mechanism of the 2011 March 04 event determined by this study. The circle in the lower left has a radius of 5 km for scale. The two dashed ellipses show the mesoseismal areas of two large earthquakes of 1863 and 1896 (Berberian & Yeats 1999). The box marks the alignment of epicentres that closely follow the arcuate shape of an E–W valley that cuts across the range at the latitude of 37.5°N. The same pattern can be seen in another branch a bit further south which includes the 2006 November 05 and 2002 January 05 earthquakes. The dashed line in the west of Sangavar Fault marks a previously unknown fault inferred from some of the well-located events.

and 71 independent station-phases. The arrival times of P_g and S_g in this distance range is very well fit with traveltimes calculated from a two-layered crustal model (Fig. 7b). The semi-axes of the 90 per cent confidence ellipse of the hypocentroid are 1.1 and 0.9 km in length and the longer axis has an azimuth of −57.3°. The final estimates of location errors for the events range from 1 to 6 km with most being less than 3 km. The result of the HDC analysis for this cluster is listed in Table 4. The confidence ellipses in Table 4 are for absolute location at the 90 per cent confidence level. Fig. 9 shows the relocated epicentres of the northern cluster. Each event is shown with its 90 per cent confidence ellipse for relative relocation. The white and grey ellipses belong to the events from the EHB catalogue and the IASBS network, respectively. The location uncertainties are generally larger for offshore events because of poorer azimuthal coverage.

Depth determination

By minimizing the residuals of direct P_g and S_g arrival times of the near stations and S_g–P_g differential times of the closely BHRC stations, we calibrated the depths of 57 events (Tables 3 and 4 and Fig. 10a). The S_g–P_g accelerometer readings were used to calibrate the depths of 28 events in the southern cluster. Among those, 10 are in the Talesh region and the rest belong to the Golestan-Ardebil cluster. For 13 of the events the focal depth was estimated using P_g and S_g readings of the shorter epicentral distances of the IASBS network. Estimated focal depths are in the 8–43 km range with average being around 14 km. This result is in close agreement with the default depth of 14 km assumed for the cluster. The observed depth range in the Caspian margin suggests that the seismogenic
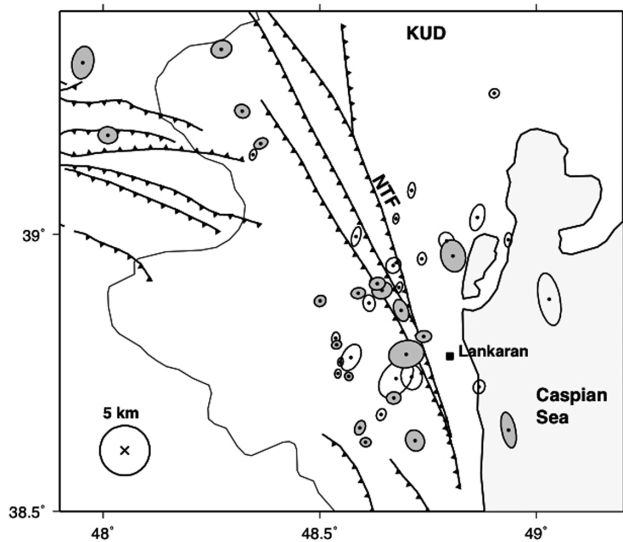
Figure 9. Epicentres of the earthquakes in the northern cluster relocated by the HDC analysis. Figure details are as in Fig. 8. The effect of relocation is generally to tighten the clustering of epicentres. The thin black line is the Azerbaijan-Iran border. NTF is the North Talesh Fault.

layer here is somewhat deeper than in the Alborz where seismic activity occurs primarily in the upper crust (Engdahl *et al.* 2006).

For a subset of 16 events of the northern cluster, we estimated focal depths using P_g and S_g readings from the Azerbaijan Seismic Network (Fig. 10a and Table 4). The depths are in the 22–42 km range, indicating a rather deep seismogenic layer. They are also in good agreement with the default depth of 26 km for this cluster.

We used pP-P and sP-P time differences to estimate depths for additional 12 and 9 events in the southern (Table 3) and northern (Table 4) clusters, respectively. Fig. 10(b) shows the distribution of the calculated depths using teleseismic depth phases. The two

different methods concur on spatial distribution and depth range comfortably.

The depth range calculated from nearby stations is in close agreement with the four depth estimates calculated from body waveform fitting by Priestley *et al.* (1994) and Jackson *et al.* (2002). The depth estimate of 15 km for the 1980 May 4 event by the above authors is rather far from our estimate of 22 km based on teleseismic relative pP-P and sP-P phases (Table 3). For this event there was no nearby station at the time to make a direct estimate.

EARTHQUAKE FOCAL MECHANISM

Fig. 2 shows the focal mechanism solutions of Jackson *et al.* (2002), and the double-couple part of the CMT focal mechanisms of large events in the study region. There is a very good agreement between the two sets of solutions. No fewer than 9 of the 13 solutions substantiate north-trending west-dipping low-angle thrust faults. The epicentres in the northern region and offshore of the Talesh do not show sharp linear trends (Figs 8 and 9) and are perhaps more consistent with low-angle fault planes with broader distribution of epicentres. Only two focal mechanisms (the 2002 January 5 and 2006 January 5 events) near the southern end of the Talesh, where the mountain range swings towards the east, show strike-slip motion.

Using waveforms of the regional INSN stations, and the method described by Dahm *et al.* (1999), we performed a waveform modelling analysis to derive the moment tensor mechanism of event 2011 March 04 ($M_L = 4.2$) that struck the region between the Sangavar and Boghrov Dag Faults. The waveforms were bandpass filtered for 20–50 s. Fig. 11 shows the details of the best-fitting moment tensor solution and the focal mechanism of the event is shown in Figs 2 and 8. We calculated the 1-D Green's functions using the reflectivity method (Muller 1985) and a crustal velocity model listed in Table 1. The impact of unknown structural complexities
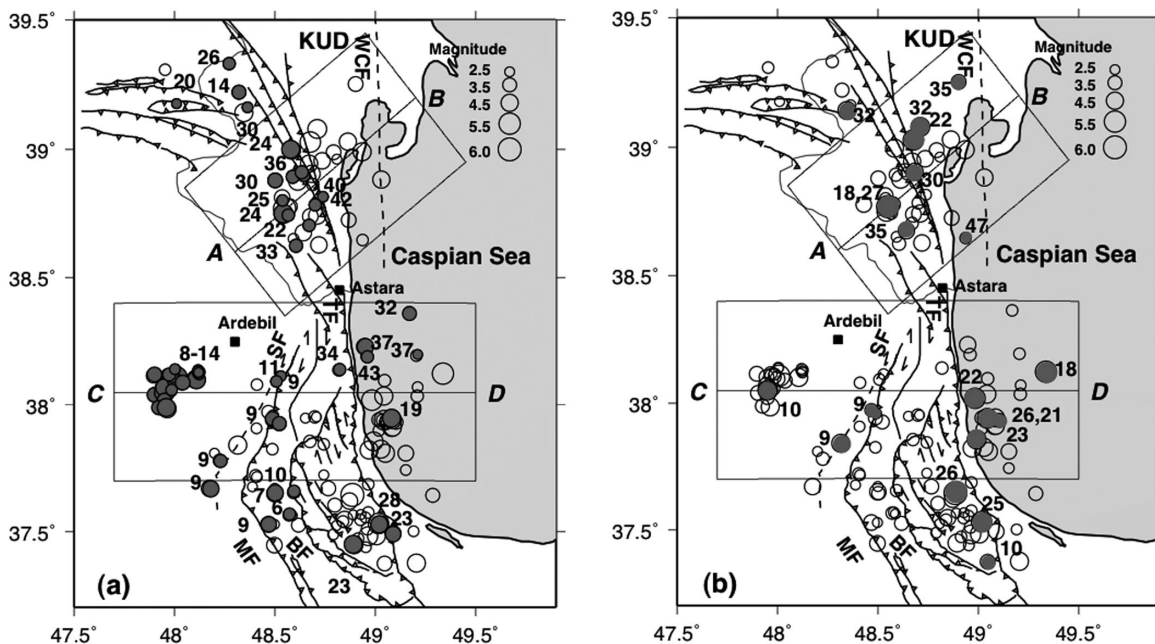

Figure 10. The depth distribution of earthquakes in the study region. Epicentres of HDC relocated events in the two clusters are shown as circles with sizes proportional to local magnitudes. (a) Those events having depth calculated from near stations are shown in grey. The numbers next to circles are estimated depths. For sake of clarity, only the depth range for events in the Golestan-Ardebil cluster is shown. (b) Events whose depths were calculated from relative teleseismic pP-P and sP-P phases are shown in grey. The swath profiles along lines AB and CD are shown in Fig. 12.
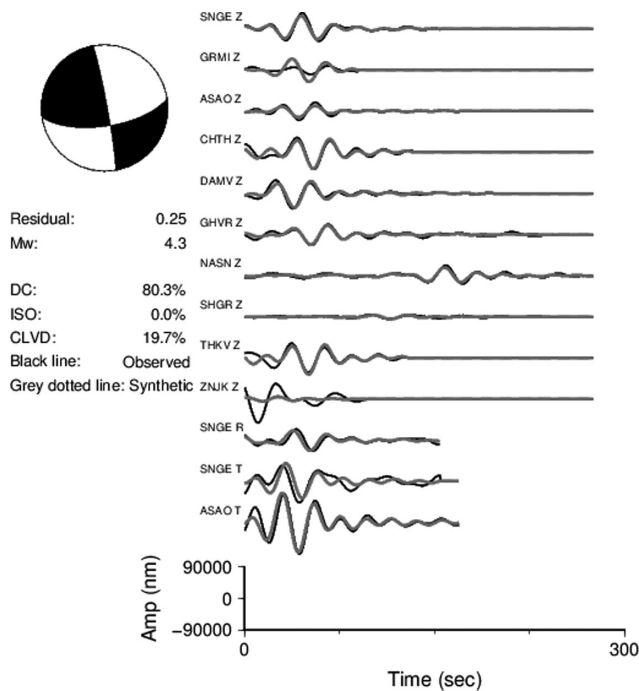
Figure 11. Minimum misfit solution for the 2011 March 4 event and comparison of the observed and predicted time series from the best-fitting amplitude spectrum inversion. The pass-band used in the inversion is 20–50 s. The vertical and horizontal axes at the bottom show amplitude (nm) and time (s) scales, respectively. The depth was fixed at 7 km. The beachball is shown in Fig. 8.

can be significant at the periods used here (Dahm *et al.* 2007), but good azimuthal distribution of stations should minimize bias from these effects.

DISCUSSIONS

One of the main questions addressed in our work is the existence of a significant level of offshore seismicity along the western border of the SCB (Figs 2, 8 and 9). In the 2 yr period of monitoring reported here, more than a quarter of the events recorded in the Talesh and the Caspian Sea are offshore events. Given the constraints, we have placed on location uncertainty, most of the offshore seismicity could not be attributed to the Talesh region. It is evident that the offshore seismicity involves many of the larger events. Figs 8 and 9 indicate that a rather broad marginal zone (~50 km wide) of the SCB is involved in major faulting activity. This seismicity quickly falls off east of the west-dipping Talesh Fault in the central Talesh, and cannot be related to that fault. There is no strong indication that the inferred vertical right-lateral WCF has any association with the offshore seismicity. The WCF has been suggested to exist north of the Talesh Mountains in the Kura Depression but its continuation in the south is still unclear.

Through the depth determination procedure described above, we have estimated numerous well-constrained focal depth values ranging from 18 to 47 km, over a long stretch from southernmost Talesh (37.4°N) to the southern margins of the Kura region (39.2°N). These depths show a consistent pattern and indicate that there is an extensive underthrusting of the Caspian basement as discussed below.

In the northern structural arc of the Talesh, the relocated events tend to be concentrated in the eastern part of the range where the

major west-dipping thrust faults are located (Figs 9 and 10). Several of these events have occurred well to the east of the thrust faults. Fig. 12a shows a swath profile (line AB in Fig. 10) of well-constrained focal depths through the Talesh and the Kura Depression. The profile clearly shows that shallow crustal seismicity is scarce and most of the events are deeper than 20 km. This pattern indicates that the deformation is dominated by the faulting of the South Caspian slab beneath the Talesh and Kura. Judging from the lateral extent of seismicity near the Talesh-Caspian margin seen in Figs 10(b) and 12(a), it appears that the Caspian slab has advanced by about 20–25 km underneath the Talesh (in Fig. 12a, we have delineated the approximate position and depth of the basement slab based on the depth distribution of the earthquakes). This is in broad agreement with the estimated 25 km of crustal shortening since late Miocene in the northern Talesh (Jackson *et al.* 2002). Fig. 12(a) also shows events (triangles) for which focal mechanisms are available. These events occur at the 27–32 km depth range and indicate faulting near the surface of the slab and/or base of the overlying layer. The rest of the events show a depth distribution inside the basement slab and are not restricted to its top surface. This is indicative of internal deformation of the slab and can give an estimate of its thickness. The large depth interval (from 20 to 45 km) of the events inside the Caspian basement suggests that the Caspian crust is very thick, and also rigid and strong. Previous work (e.g. Mangino & Priestley 1998) has shown that the Caspian basement sharply thickens towards its western margins (20 km over 100 km). The observed depth of seismicity lends support to the notion of a thick crust under the Caspian Sea.

A similar picture can be seen further south. Fig. 12(b) shows a swath profile through the central and southern Talesh and the Caspian Sea (line CD in Fig. 10). It shows two distinct clusters of earthquakes. The deeper events, ranging in depth from 18 to 43 km, occur in the basement of the Caspian slab. The events of the shallower cluster in the west are all in the western flank of the Talesh and in regions further west, and represent the seismic deformation of the upper continental crust. The amount of underthrusting of the Caspian basement beneath the central Talesh appears to be more limited compared to the northern Talesh. In Figs 10 and 12(b), only 2 or 3 of the deeper events have occurred in the west of the Talesh Fault and it is not clear whether or not the central Talesh is underlain by the Caspian basement.

Inside the Talesh Mountains, seismicity tends to be concentrated in the northern and southern arcuate parts of the range, with the central region being considerably less seismic (Figs 2 and 10). This is in agreement with the variable intensity of deformation along the mountain range, as described in the previous section. A prominent feature in the relocated events with depth constraint is that shallow events are absent in the eastern flank of the mountain range throughout its entire length. This does not mean that the upper crust is aseismic, rather it suggests that seismicity is concentrated in the lower crust of the Talesh and the basement slab of the Caspian. Shallow events are restricted to the western flank of the southern Talesh, where their average depth is around 10 km. Some of these events are in the hanging wall of the Masuleh and Sangavar Faults, and the rest are in the footwall of the Sangavar Fault, which are in fact outside of the Talesh range. Due to the small number of well-located events and few focal mechanism solutions we cannot precisely relate the epicentres to the mapped faults in the region. Nevertheless, concentration of upper crustal seismicity around the Sangavar Fault suggests that this fault may have a role in the right-lateral northward motion of the Talesh relative to the SCB.
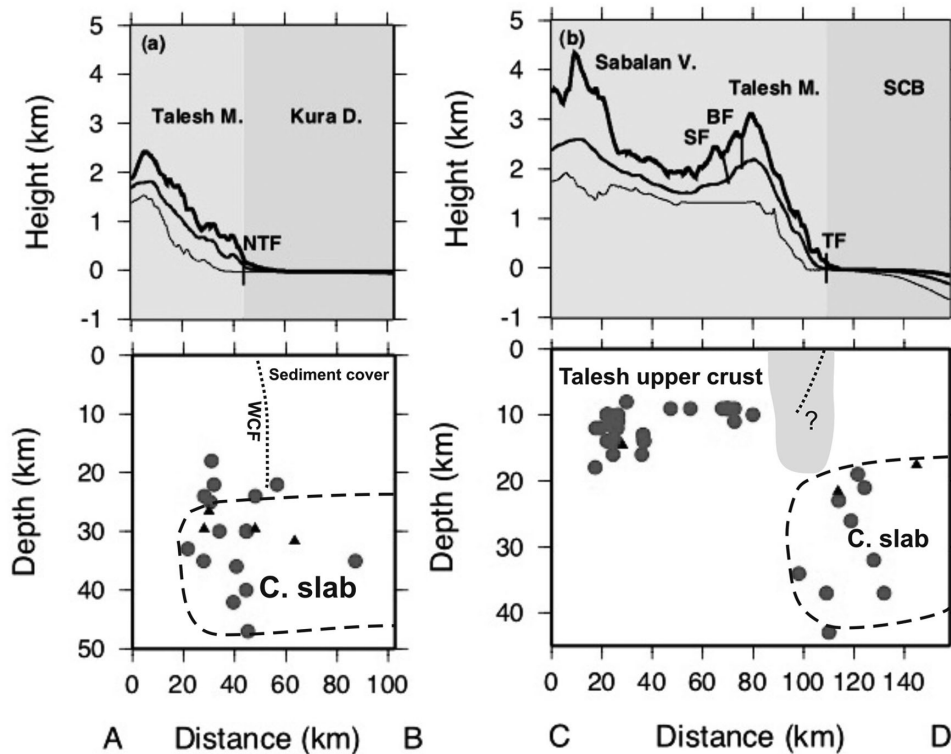
Figure 12. The swath profile of the topography and hypocentres along the AB profile (a) and CD profile (b) shown in Fig. 10. The triangles are events for which a Harvard CMT solution is available (Fig. 2). The maximum (thick line), minimum (thin line), and mean (medium size line) elevations were extracted from the rectangular windows in Fig. 10. The dashed lines mark the basement slab of the west Caspian as inferred from the seismicity data. The position of WCF is taken from the interprerted cross-section in Allen *et al.* (2003). Those authors interpret this fault as a boundary separating the Caspian sedimentary basin from the Talesh continental crust. The shaded area in (b) marks the aseismic region beneath the central Talesh. Topography data source: ETOPO1, 1 Arc-Minute Global Relief Model, Amante & Eakins (2009). Abbreviations: TF (Talesh Fault), SF (Sangavar Fault) and BF (Boghrov Dag Fault).

Two historical earthquakes have been associated with the NNE-trending high-angle Sangavar Fault, the northern segment of the Masuleh Fault (Ambraseys & Melville 1982) (Fig. 8). The first earthquake (magnitude ∼6.1) ruptured the northern segment of the fault in 1863. The second earthquake (magnitude ∼6.7) ruptured the southern segment in 1896 (Berberian & Yeats 1999). The mezo-seismal zones are shown in Fig. 8. Close alignment of numerous well-located events with the trace of the fault is further evidence of its seismically active state.

The 2011 March 4 event ($M_L = 4.2$) lies between the Boghrov Dag and Sangavar Faults (Fig. 8). As far as we can determine, there is no known fault in this region. We have determined a strike-slip mechanism for the event. The near-vertical fault planes in the solution discourage us from associating it with the Masuleh reverse fault. The N-trending right-lateral fault plane is in good agreement with the general trends of the known faults in the region and with the expected right-lateral sense of motion. In addition, the event lies within a NNW-trending valley. This evidence implies the existence of an unrecognized fault in this region.

To the west of the Sangavar Fault there is another alignment of events trending NE–SW. The majority of the events have focal depth of about 9 km (the dashed line in Fig. 8). No corresponding fault has been mapped in this region and this observation warrants further investigation to seek evidence for active deformation.

In the southern Talesh Mountains, around the 37.5° latitude, there is an E–W arc-like alignment of epicentres of small events (black box in Fig. 8). The alignment closely follows the course of an E–W valley (Poonel Road) that cuts through the mountain range. These events may be related to an unknown fault. Madanipour *et al.* (in

preparation) observed fault exposures with a strike-slip sense of motion in a few road cuts along the Poonel road but they could not find evidence of active tectonics.

CONCLUSIONS

In this work, we have explored the existence of offshore seismicity in the western part of the SCB, obtaining bias-free locations through an advanced multiple-event relocation analysis based on local distance readings from a temporary seismograph network. The pattern of seismicity cannot be associated with the known on-shore faults (e.g. the Talesh Fault) or proposed offshore faults (e.g. the WCF). Major earthquake clusters on shore correspond to the northern and southern structural bends of the Talesh Mountains, and signify intense deformation in those regions. From the depth distribution of the well-located events, we infer that the basement of the Caspian Basin accounts for a major part of the seismicity in the region. The hypocentral depths along the southwestern margin of the Caspian reach to 47 km. This signifies a rather deep underthrusting of the South Caspian beneath the northern Talesh, however, the depth of seismicity is significantly lower than in the Apsheron-Balkhan sill where earthquakes as deep as 80 km occur and the SCB there is believed to be subducting under Eurasia. In central and southern Talesh, the extent of underthrusting is even less than in the northern Talesh. Therefore, if there is subduction of the SCB along its western margin, it is still in an earlier stage. The low level of shallow seismicity, especially on the eastern side of the Talesh, is puzzling, given the intensity and complexity of the

structures and interactions of the tectonic blocks involved. The seismicity accompanying the thrust faulting in the underlying Caspian basement does not continue to the upper crust of the Talesh. Furthermore, despite strong evidence that there should be a significant N–S right-lateral strike-slip motion in the Talesh, there is no trend in the seismicity to delineate a single N–S structure. Therefore, as Jackson *et al.* (2002) have suggested, it is possible that the right-lateral shear deformation may be distributed over a wedge of sediment cover, instead of on a single, deep-cutting fault structure. A newly calculated strike-slip focal mechanism, distribution of well-located earthquakes and geological field work suggest that in the western margins of the southern Talesh, right-lateral motion is accommodated on a number of NE–SW trending faults, both known and unknown.

In northern Talesh most of the relocated seismicity occurs in the eastern part of the range, indicating that deformation is presently concentrated in the eastern flank. Furthermore, the deep seismicity indicates the underthrusting of an oceanic type of crust of the Kura Depression beneath the Talesh.

ACKNOWLEDGEMENTS

REFERENCES

Allen, M.B., Vincent, S.J., Alsop, I., Ismail-zadeh, A. & Flecker, R., 2003. Late Cenozoic deformation in the South Caspian region: effects of a rigid basement block within a collision zone, *Tectonophysics,* **366,** 223–239.

Amante, C. & Eakins, B.W., 2009. *ETOPO1 1 Arc-Minute Global Relief Model: Procedures, Data Sources and Analysis,* NOAA Technical Memorandum NESDIS NGDC 24, 19 pp.

Ambraseys, N.N. & Melville, C.P., 1982. *A History of Persian Earthquakes,* Cambridge University Press, 240 pp.

Berberian, M., 1983. The southern Caspian: a compressional depression floored by a trapped, modified oceanic crust, *Can. J. Earth Sci.,* **20,** 163–183.

Berberian, M. & Yeats, R.S., 1999. Patterns of historical earthquake rupture in the Iranian plateau, *Bull. seism. Soc. Am.,* **89,** 120–139.

Biggs, J., Bergman, E., Emmerson, B., Funning, G., Jackson, J., Parsons, B. & Wright, T., 2006. Fault identification for buried strike-slip earthquakes using InSAR: the s1994 and 2004 Al Hoceima, Morocco earthquakes, *Geophys. J. Int.,* **166,** 1347–1362.

Bondar, I., Bergman, E.A., Engdahl, E.R., Kohl, B., Kung, Y.L. & McLaughlin, K., 2008. A hybrid multiple event location technique to obtain ground truth event locations, *Geophys. J. Int.,* **175,** 185–201.

Brunet, M.F., Korotaev, M.V., Ershov, A.V. & Nikishin, A.M., 2003. The South Caspian Basin: a review of its evolution from subsidence modeling, *Sedimentary Geol.,* **156,** 119–148.

Croux, C. & Rousseeuw, P.J., 1992. Time-efficient algorithms for two highly robust estimators of scale, *Comput. Stat.,* **1,** 411–428.

Dahm, T., Kruger, F., Stammler, K., Kinge, K., Kind, R., Wylegalla, K. & Grasso, J.R., 2007. The 2004 Mw 4.4 Rotenburg, northern Germany, earthquake and its possible relationship with gas recovery, *Bull. seism. Soc. Am.,* **97,** 691–704.

Dahm, T., Manthei, G. & Eisenblätter, J., 1999. Automated moment tensor inversion to estimate source mechanisms of hydraulically induced microseismicity in salt rock, *Tectonophysics,* **306,** 1–17.

Davies, R.G., Jones, C.R., Hamzepour, B. & Clark, G.C., 1972. *Geology of the Masuleh Sheet (1:100,000), Northwest Iran,* Technical Report, Geological Survey of Iran, 110 pp.

Devlin, W.J., Cogswell, J.M., Gaskins, G.M., Jaksen, G.H., Pitcher, D.M., Puls, D.P., Stanley, K.O. & Wall, G.R.T., 1999. South Caspian basin: young, cool, and full of promise, *GSA Today,* **9**(7), 1–9.

Djamour, Y., Vernant, P., Nankali, H.R. & Tavakoli, F., 2011. NW Iran-eastern Turkey present-day kinematics: results from the Iranian permanent GPS network, *Earth planet. Sci. Lett.,* **307,** 27–34.

Djamour, Y. *et al.*, 2010. GPS and gravity constraints on continental deformation in the Alborz Mountain range, Iran, *Geophys. J. Int.,* **183,** 1287–1301.

Doloei, J. & Roberts, R., 2003. Crustal and uppermost mantle structure of Tehran region from teleseismic P-waveform receiver function analysis, *Tectonophysics,* **364,** 115–133.

Engdahl, E.R., Van der Hilst, R. & Buland, R., 1998. Global teleseismic earthquake relocation with improved travel times and procedures for depth determination, *Bull. seism. Soc. Am.,* **88,** 722–743.

Engdahl, E.R., Jackson, J.A., Myers, S.C., Bergman, E.A. & Priestley, K., 2006. Relocation and assessment of seismicity in the Iran region, *Geophys. J. Int.,* **167,** 761–778.

Ghods, A., Rezapour, M., Bergman, E., Mortezanejad, G. & Talebian, M., 2012. Relocation of the 2006 Mw 6.1 Silakhour, Iran, earthquake sequence: details of fault segmentation on the main recent fault, *Bull. seism. Soc. Am.,* **102**(1), 398–416.

Ghods, A. & Sobouti, F., 2005. Quality assessment of seismic recording: Tehran Seismic Telemetry Network, *Asian J. Earth Sci.,* **25,** 687–694.

Havskov, J. & Otemoller, L., 1999. *SEISAN: The Earthquake Analysis Software,* version 8.0, Institute of Solid Earth Physics, University of Bergen.

Hutton, L.K. & Boore, D.M., 1987. The ML scale in southern California, *Bull. seism. Soc. Am.,* **77,** 2074–2094.

Jackson, J. & McKenzie, D., 1984. Active tectonics of the Alpine-Himalayan Belt between western Turkey and Pakistan, *Geophys. J. R. Astr. Soc.,* **77,** 185–264.

Jackson, J., Haines, J. & Holt, W., 1995. The accommodation of Arabia-Eurasia plate convergence in Iran, *J. geophys. Res.,* **100**(B8), 15205–15219.

Jackson, J., Priestley, K. & Berberian, M., 2002. Active tectonics of the South Caspian Basin, *Geophys. J. Int.,* **148,** 214–245.

Jordan, T.H. & Sverdrup, K.A., 1981. Teleseismic location techniques and their application to earthquake clusters in the south-central Pacific, *Bull. seism. Soc. Am.,* **71,** 1105–1130.

Hessami, K., Jamali, F. & Tabassi, H., 2003. *Major Active Faults of Iran (map),* scale 1:2,5000,000, Ministry of Science, Research and Technology, International Institute of Earthquake Engineering and Seismology.

Kadirov, F., Floyd, M., Alizadeh, A., Guliev, I., Reilinger, R., Kuleli, S., King, R. & Toksoz, N., 2012. Kinematics of the Caucasus near Baku, Azerbaijan, *Nat. Hazards,* **63,** 997–1006.

Kaviani, A., 2004. La chaine de collision continentale du Zagros (Iran): structure litospherique par analyse De donees sismologiques, *PhD Thesis,* University of Joseph Fourier-Grenoble I.

Kaz'min, V.G. & Verzhbitskii, E.V., 2011. Age and origin of the South Caspian Basin, *Earth Environ. Sci.,* **51,** 131–140.

Khain, V.Y., Grigoryants, B.W. & Isayev, B.M, 1966. The West Caspian Fault and factors governing the formation of transverse faults in geosynclinal fold belts, *MOIP Bull.,* **41,** 5–23.

Knapp, J.H. & Connor, J.A., 2004. Crustal-scale structure of the South Caspian Basin revealed by deep seismic reflection profiling, *Marine Petrol. Geol.,* **21,** 1073–1081.

Lienert, B.R. & Havskov, J., 1995. A computer program for locating earthquakes both locally and globally, *Seismol. Res. Lett.,* **66,** 26–36.

Mangino, S. & Priestley, K., 1998. The crustal structure of the southern Caspian region, *Geophys. J. Int.,* **133**(3), 630–648.

Muller, G., 1985. The reflectivity method: a tutorial, *J. Geophys.,* **58,** 153–174.

Parsons, B. *et al.*, 2006. The 1994 Sefidabeh (eastern Iran) earthquakes revisited: new evidence from satellite radar interferometry and carbonate

dating about the growth of an active fold above a blind thrust fault, *Geophys. J. Int.,* **164,** 202–217.

Priestley, K., Baker, C. & Jackson, J., 1994. Implications of earthquake focal mechanism data for the active tectonics of the South Caspian Basin and surrounding regions, *Geophys. J. Int.,* **118,** 111–141.

Tatar, M., Jackson, J., Hatzfeld, D. & Bergman, E.A., 2007. The 28 May 2004 Baladeh earthquake (Mw 6.2) in the Alborz, Iran: implications for the geology of the south Caspian basin margin and for the seismic hazard of Tehran, *Geophys J. Int.,* **170,** 249–261.

Tatar, M., 2001. Etude siesmotectonique de deux zones de collision continentale: Le Zagros Central et l'Alborz (Iran), *PhD Thesis,* University of Joseph Fourier-Grenoble I.

Walker, R.T., Bergman, E., Jackson, J., Ghorashi, M. & Talebian, M.,

2005. The 2002 June 22 Changureh (Avaj) earthquake in Qazvin Province, northwest Iran: epicentral relocation, source parameters, surface deformation and geomorphology, *Geophys. J. Int.,* **160,** 707–720.

Walker, R.T., Bergman, E.A., Szeliga, W. & Fielding, E.J., 2011. Insights into the 1968–1997 Dasht-e-Bayaz and Zirkuh earthquake sequences, eastern Iran, from calibrated relocations, InSAR and high-resolution satellite imagery, *Geophys. J. Int.,* **187,** 1577–1603.

Walker, R.T. *et al.*, 2013. The 2010–2011 South Rigan (Baluchestan) earthquake sequence and its implications for distributed deformation and earthquake hazard in southeast Iran, *Geophys. J. Int.,* **193,** 349–374.

Wessel, P. & Smith, W.H.F., 1998. New, improved version of the Generic Mapping Tools released, *EOS Trans. AGU,* **79,** 579.